

Big Three Dragons: A [N II] 122 μm Constraint and New Dust-continuum Detection of A $z = 7.15$ Bright Lyman Break Galaxy with ALMA

YUMA SUGAHARA,^{1,2} AKIO K. INOUE,^{2,3} TAKUYA HASHIMOTO,⁴ SATOSHI YAMANAKA,^{2,5} SEIJI FUJIMOTO,^{6,7} YOICHI TAMURA,⁸
HIROSHI MATSUO,^{1,9} CHRISTIAN BINGGELI,¹⁰ AND ERIK ZACKRISSON¹⁰

¹National Astronomical Observatory of Japan, 2-21-1 Osawa, Mitaka, Tokyo 181-8588, Japan

²Waseda Research Institute for Science and Engineering, Faculty of Science and Engineering, Waseda University, 3-4-1, Okubo, Shinjuku, Tokyo 169-8555, Japan

³Department of Physics, School of Advanced Science and Engineering, Faculty of Science and Engineering, Waseda University, 3-4-1, Okubo, Shinjuku, Tokyo 169-8555, Japan

⁴Tomonaga Center for the History of the Universe (TCHoU), Faculty of Pure and Applied Sciences, University of Tsukuba, Tsukuba, Ibaraki 305-8571, Japan

⁵Research Center for Space and Cosmic Evolution, Ehime University, 2-5 Bunkyo-cho, Matsuyama, Ehime 790-8577, Japan

⁶Cosmic Dawn Center (DAWN), Jagtvej 128, DK2200 Copenhagen N, Denmark

⁷Niels Bohr Institute, University of Copenhagen, Lyngbyvej 2, DK2100 Copenhagen, Denmark

⁸Division of Particle and Astrophysical Science, Graduate School of Science, Nagoya University, Nagoya 464-8602, Japan

⁹The Graduate University for Advanced Studies (SOKENDAI), 2-21-1, Osawa, Mitaka, Tokyo 181-8588, Japan

¹⁰Observational Astrophysics, Department of Physics and Astronomy, Uppsala University, Box 516, SE-751 20 Uppsala, Sweden

Submitted to ApJ

ABSTRACT

We present new Atacama Large Millimeter/submillimeter Array Band 7 observational results of a Lyman break galaxy at $z = 7.15$, B14-65666 (“Big Three Dragons”), which is an object detected in [O III] 88 μm , [C II] 158 μm , and dust-continuum emission during the epoch of reionization. Our targets are the [N II] 122 μm fine-structure emission line and underlying 120 μm dust continuum. The dust continuum is detected with a $\sim 19\sigma$ significance. From far-infrared spectral energy distribution sampled at 90, 120, and 160 μm , we obtain a best-fit dust temperature of 40 K (79 K) and an infrared luminosity of $\log_{10}(L_{\text{IR}}/L_{\odot}) = 11.6$ (12.1) at the emissivity index $\beta = 2.0$ (1.0). The [N II] 122 μm line is not detected. The 3σ upper limit of the [N II] luminosity is $8.1 \times 10^7 L_{\odot}$. From the [N II], [O III], and [C II] line luminosities, we use the Cloudy photoionization code to estimate nebular parameters as functions of metallicity. If the metallicity of the galaxy is high ($Z > 0.4 Z_{\odot}$), the ionization parameter and hydrogen density are $\log_{10} U \simeq -2.7 \pm 0.1$ and $n_{\text{H}} \simeq 50\text{--}250 \text{ cm}^{-3}$, respectively, which are comparable to those measured in low-redshift galaxies. The nitrogen-to-oxygen abundance ratio, N/O, is constrained to be sub-solar. At $Z < 0.4 Z_{\odot}$, the allowed U drastically increases as the assumed metallicity decreases. For high ionization parameters, the N/O constraint becomes weak. Finally, our Cloudy models predict the location of B14-65666 on the BPT diagram, thereby allowing a comparison with low-redshift galaxies.

Keywords: galaxies: formation; galaxies: evolution; galaxies: ISM; galaxies: high-redshift galaxies

1. INTRODUCTION

The Atacama Large Millimeter/submillimeter Array (ALMA) has contributed to several pioneering works on far-infrared (FIR) fine-structure lines in star-forming galaxies at redshift $z > 7$, providing new insights into galaxy formation and evolution at the earliest epochs. The [C II] 158 μm emission line, one of the brightest emission lines in the FIR band, is commonly used to trace high-redshift galaxy properties (e.g., Capak et al. 2015; Carniani et al. 2018; Le Fèvre et al.

2019; Bakx et al. 2020), even at $z > 7$ (Maiolino et al. 2015; Pentericci et al. 2016; Hashimoto et al. 2019; Carniani et al. 2020). While the [C II] line is a dominant coolant in neutral gas (Tielens & Hollenbach 1985; Abel et al. 2005) and relevant to star-forming activities (e.g., Boselli et al. 2002; De Looze et al. 2014; Schaerer et al. 2020; Fujimoto et al. 2021), the low ionization potential of C^+ (11.3 eV) permits [C II] emission in various phases: H II regions, photodissociated regions (PDRs), cold neutral and molecular medium, and shocks caused by galaxy interactions (e.g., Russell et al. 1980; Tielens & Hollenbach 1985; Appleton et al. 2013). The [O III] 88 μm is another tracer for high-redshift star formation (Inoue et al. 2014) and has also been detected at $z \gtrsim 7$

(Inoue et al. 2016; Carniani et al. 2017; Laporte et al. 2017; Marrone et al. 2018; Hashimoto et al. 2018, 2019; Tamura et al. 2019). In contrast to the [C II] line, the [O III] line arises only from H II regions due to high ionization potential of O^{2+} (35.1eV). The combination of these two FIR lines provides information on the physical conditions of the interstellar medium (ISM) in individual high-redshift galaxies, which are difficult to probe with weak nebular emission lines in the rest-frame ultraviolet (UV) band. Inoue et al. (2016) found a deficit in [C II]-to-[O III] luminosity ratios compared with local galaxies, possibly suggesting a highly ionized state in high-redshift galaxies. This is supported by recent observational studies (Hashimoto et al. 2019; Harikane et al. 2020; but see Carniani et al. 2020)

In addition to fine-structure lines, high sensitivity observations with ALMA enable the detection of FIR continuum emission at $z > 7$ (Watson et al. 2015; Laporte et al. 2017; Hashimoto et al. 2019; Tamura et al. 2019). Infrared luminosity is dominated by thermal dust emission, reflecting UV energy absorbed by dust. Dust attenuation at high-redshift is essential for understanding intrinsic galaxy properties. Several previous studies have assessed dust attenuation using the relation between infrared excess and UV spectral slopes (the IRX- β_{UV} relation; Meurer et al. 1999; Watson et al. 2015; Bouwens et al. 2016; Bowler et al. 2018; Hashimoto et al. 2019; Harikane et al. 2020; Fudamoto et al. 2020). FIR spectral energy distribution (SED) is another clue for constraining dust properties, including dust temperature and dust mass. Bakx et al. (2020) reported the non-detection of dust continuum at 160 μm in a Lyman break galaxy (LBG) at $z = 8.3113$, MACS0416_Y1, despite detecting it at 90 μm . These results suggest an unusually high dust temperature $T_{\text{dust}} > 80$ K or a high emissivity index $\beta > 2$. While FIR SED is usually fitted by a modified blackbody function with an assumed dust temperature, Inoue et al. (2020) proposed a new algorithm for determining dust temperature based on radiative equilibrium on dust grains.

This paper presents new observations of an LBG, B14-65666, which is the first example of a galaxy detected in [O III] 88 μm , [C II] 158 μm , and underlying dust continuum at the epoch of reionization (so-called ‘‘Big Three Dragons,’’ Hashimoto et al. 2019) in order to take a step further in understanding galaxy properties at high-redshift. The new observations are used to detect another FIR emission line [N II] 122 μm (2459.380 GHz¹) and underlying dust continuum at 120 μm . An additional dust continuum measurement is useful for constraining dust properties. Observations of [N II] lines are limited at high-redshift, but the number of detections has been increasing. [NII] 122 μm lines are detected in quasars at $z = 7.54$ (Novak et al. 2019) and at $z = 6.003$ (Li et al. 2020), a dusty star-forming galaxy (DSFG) at $z = 4.22$ (De Breuck et al. 2019), and a submillimeter galaxy (SMG)

and quasar system at $z = 4.69$ (Lee et al. 2019), whereas Harikane et al. (2020) reported three LBGs at $z \sim 6$ that are not detected in [N II] 122 μm lines despite detecting them in [C II] and [O III] lines. In another excitation state, [N II] 205 μm lines are detected in galaxies at $z = 5\text{--}6$ (Pavesi et al. 2016), SMGs at $3 < z < 6$ (Cunningham et al. 2020), and $z > 4$ objects, including quasars and DSFGs (e.g., Decarli et al. 2014; De Breuck et al. 2019; Novak et al. 2019; Cheng et al. 2020).

It is important to study galaxy ISM with emission-line diagnostics thorough a wide range of redshifts at $z = 0\text{--}7$. At $z = 0\text{--}2$, physical properties in star-forming galaxies are probed in detail using rest-frame optical emission lines. The optical wavelength range includes emission lines from different elements (e.g., H, O, N, S), excited states (e.g., [N II] $\lambda\lambda 6549, 6585$), and ionization states (e.g., O^+ and O^{2+}); thus, temperatures, densities, elemental abundances, and ionizing sources in H II regions can be inferred by comparing emission-line fluxes. The nitrogen-to-oxygen (N/O) abundance ratio provides a clue to the chemical evolution in galaxies (e.g., Vincenzo et al. 2016) because more nitrogen is produced through the carbon-nitrogen-oxygen (CNO) cycle as a secondary nucleosynthesis product in stars with higher metallicity. Among dominant ionizing sources of strong line emitters, star-formation and active galactic nuclei (AGNs) can be distinguished on the [O III]/ $H\beta$ –[N II]/ $H\alpha$ plane, the so-called Baldwin-Phillips-Terlevich (BPT) diagram (Baldwin et al. 1981; Veilleux & Osterbrock 1987). The distribution on the BPT diagram is theoretically interpreted as a combination of the nebular physical parameters and hardness of ionizing radiation (Kewley et al. 2013).

Galaxy properties at $z = 2$ have been explored using near-infrared (NIR) instruments to detect redshifted optical lines. On the BPT diagram, the sequence of star-forming galaxies at $z \sim 2$ has an offset from the local sequence (e.g., Shapley et al. 2005; Erb et al. 2006), which is statistically confirmed using the KBSS-MOSFIRE sample (Steidel et al. 2014, 2016; Strom et al. 2017), the MOSDEF sample (Shapley et al. 2015; Sanders et al. 2016; Shivaiei et al. 2018), and Subaru/FMOS observations (Yabe et al. 2014; Hayashi et al. 2015; Kashino et al. 2017). This offset on the BPT diagram originates from the redshift evolution of ionization states in star-forming galaxies. Strom et al. (2018) derived the N/O abundance ratios of KBSS-MOSFIRE galaxies to find that the N/O ratio at $z \sim 2$ is comparable with local abundance ratios (Pilyugin et al. 2012) at fixed metallicities even though an increase in the N/O ratio is suggested from local to $z \sim 2$ in some studies (e.g., Masters et al. 2014; Sanders et al. 2016; Kojima et al. 2017).

The optical and NIR observations are powerful tools for galaxy properties, but a redshift range is limited from $z \sim 0$ to 2. We have to wait for MIR observations with the James Webb Space Telescope (JWST) to extend the studies for higher redshifts. On the other hand, FIR observations of fine-structure lines are available only for galaxies at $z > 3$ using ALMA or for local galaxies using telescopes such as Herschel, ISO, and AKARI. This redshift gap in FIR observa-

¹ This is taken from the Spectral Line Atlas of Interstellar Molecules (SLAIM) (Available at <http://www.splatalogue.net>; F. J. Lovas, private communication, Remijan et al. 2007).

tions makes it difficult to discuss a continuous galaxy evolution scenario. We propose comparisons of the physical ISM properties at various redshifts estimated from either FIR or optical emission lines to overcome this difficulty, with the aid of a photoionization model.

This paper consists of the following sections. Section 2 describes the B14-65666 observations and data reduction process. Section 3 presents the dust continuum and [N II] 122 μm emission line measurements. Section 4 explains FIR SED fittings and their results. We evaluate nebular parameters from [O III] 88 μm and [C II] 158 μm in Section 5. We discuss the N/O abundance ratio and BPT diagram at $z \sim 7$ using these nebular parameters. Section 6 summarizes our findings.

2. OBSERVATION AND DATA REDUCTION

Our target object, B14-65666, is located at RA $10^{\text{h}}01^{\text{m}}40^{\text{s}}.69$, Dec. $+01^{\circ}54'52''.42$ (J2000). It was found by Bowler et al. (2014) and spectroscopically detected in Ly α by Furusawa et al. (2016). Bowler et al. (2018) performed ALMA follow-up observations with Band 6 in Cycle 3 and reported the detection of 160 μm dust continuum. Hashimoto et al. (2019) detected [O III] 88 μm , [C II] 158 μm , and underlying dust continua in Cycles 4 and 5.

We target the [N II] 122 μm emission line, which is free from atmospheric absorption, to obtain a signature of nitrogen. The frequency (wavelength) of the line at the rest frame is 2459.380 GHz (121.898 μm). An advantage of this line is it has a similar critical density to the [O III] 88 μm (238 and 500 cm^{-3} at 10^4 K, respectively²), resulting in a weak dependence of the [N II] 122 μm /[O III] 88 μm line ratio on electron density. In contrast, the [N II] 205 μm line has a lower critical density (38 cm^{-3}) by an order of magnitude than the [O III] line, leading to a quick drop of the [N II]-to-[O III] line ratio at high density. The [N III] 57 μm line is another candidate observable with Band 9, but it takes a longer integration time to detect the line with the same significance level as the [N II] 122 μm line.

We have observed B14-65666 in 2019 November with ALMA Band 7 during Cycle 7 (ID: 2019.1.01491.S, PI: A. K. Inoue). The 12-m array was configured in the C43-2 configuration. The correlator operated in a time division mode with 2.000 GHz bandwidths and 31.2 MHz spectral resolution. One of the four spectral windows targets the [N II] 122 μm emission line at an expected frequency of 301.6885 GHz, and the others target dust continuum emission at 299.893, 289.500, and 287.700 GHz. The total on-source exposure time was 143 minutes. The bandpass/flux calibrators are quasars J1058+0133 and J0725-0054. The phase calibrator is J1010-0200.

² In this paper, the critical density for a given excited state is defined as the density at which the sum of collisional excitation and de-excitation rates balances the spontaneous emission rate. Critical densities are computed using PyNeb (Luridiana et al. 2015).

Data reduction and calibration are performed using a standard pipeline on Common Astronomy Software Applications (CASA; McMullin et al. 2007) version 5.6.1-8. A dust continuum image is created using a CASA task `tclean` with natural weighting. A line cube is created using `tclean` with a $\simeq 15.6 \text{ km s}^{-1}$ spectral resolution after the dust continuum is subtracted with a CASA task `uvcontsub`. In both the dust continuum image and line momentum 0 map (Section 3.2), the beam size is approximately $1.15'' \times 0.97''$, and the beam position angle is approximately 73° .

3. MEASUREMENTS

3.1. 120 μm Dust Continuum Emission

The left panel of Figure 1 illustrates the 120 μm dust continuum image with white contours overlaid on the *F140W*-band image taken using the Wide Field Camera 3 (WFC3) on board the Hubble Space Telescope (HST). The root mean square (rms) of the image is $\sigma = 9.8 \mu\text{Jy beam}^{-1}$. The dust continuum is significantly detected with a peak signal-to-noise ratio (S/N) of 18.9. This detection makes B14-65666 the second object in which dust continua are detected in more than two bands at $z > 7$ after A1689zD1 (Watson et al. 2015; Knudsen et al. 2017; Inoue et al. 2020). Bowler et al. (2018) suggested a physical offset of 3 kpc between the dust continuum and UV emission, but our measurement of 120 μm dust emission shows no spatial offset from UV emission on the WFC3/*F140W* image, which has consistent astrometry with the images used by Bowler et al. (2018). Although 120 μm dust emission is not spatially resolved with this beam size, our result that no spatial offset was observed is consistent with the results on 90 and 160 μm dust continua reported by Hashimoto et al. (2019).

We measure the spatially integrated flux density of the dust continuum using a 2D Gaussian profile with a CASA task `imfit`. The measured flux density is $218 \pm 19 \mu\text{Jy}$. This flux density at 120 μm is less than the continuum flux density at 90 μm ($470 \pm 128 \mu\text{Jy}$) but larger than at 160 μm ($130 \pm 25 \mu\text{Jy}$), measured in Hashimoto et al. (2019). The 120 μm flux density has a higher S/N than the 90 and 160 μm flux density by a factor of 3–4. These measurements are listed in Table 1. We examine the FIR SED with modified blackbody and radiative equilibrium models to estimate the IR luminosity based on Inoue et al. (2020) in Section 4.

3.2. Upper Limit of [N II] 122 μm Emission Line

Emission lines from ionized nitrogen, having a higher ionization potential than ionized hydrogen, arise from H II regions, as well as [O III] emission lines do. The observed-frame wavelength/frequency of [N II] 122 μm should be scaled with the same redshift as those of [O III] emission lines. We assume the observed-frame [N II] 122 μm frequency as 301.7 GHz (993.7 μm) using a systemic redshift of $z = 7.1521$, which was determined from [C II] 158 μm and [O III] 88 μm emission lines by Hashimoto et al. (2019).

We find no emission line features around the observed-frame [N II] frequency. Assuming that the [N II] line width

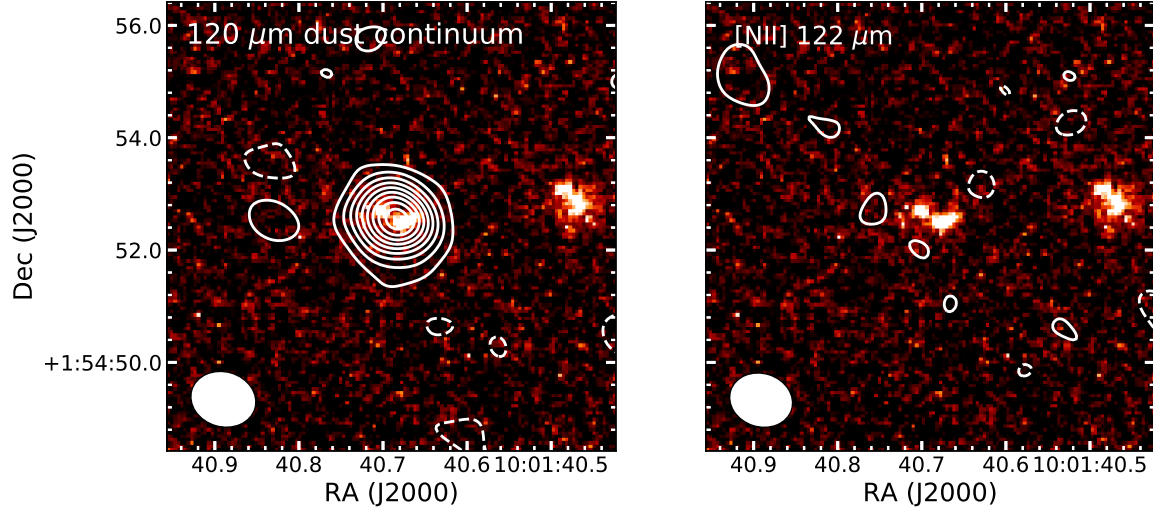


Figure 1. Left: ALMA 120 μm dust contours overlaid on the HST/WFC3 *F140W*-band pseudo-color image. The contours are drawn with 2σ intervals from the -2σ to 18σ level, where $\sigma = 9.8 \mu\text{Jy beam}^{-1}$. The white ellipse at the lower left shows the size of the synthesized beam. Right: ALMA [N II] 122 μm contours overlaid on the HST/*F140* image. The integrated velocity range for the contours is from -201 to 203 km s^{-1} with respect to the systemic redshift measured using [O III] and [C II]. The contours are drawn with -2σ and 2σ levels, where $\sigma = 17.1 \mu\text{Jy beam}^{-1}\text{km s}^{-1}$. As seen, the [N II] 122 μm emission line is not detected.

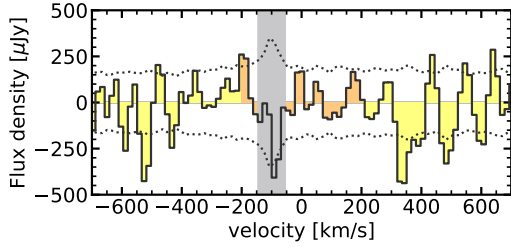


Figure 2. The spectrum around the [N II] 122 μm line, where the velocity (optical definition) is relative to the systemic redshift of $z=7.1521$ determined by Hashimoto et al. (2019). The aperture radius for the spectrum is $1''$. The dotted lines represent the noise spectrum. The range of velocities used for the [N II] 122 μm line flux is highlighted in orange. The gray region is not used to measure the [N II] line flux due to large spectral noise. As seen, the [N II] 122 μm emission line is not detected.

is $\simeq 400 \text{ km s}^{-1}$, which is close to the full-width half-maximum of [C II] and [O III] lines (Hashimoto et al. 2019), we create a [N II] flux (moment 0) map integrated from -201 to 203 km s^{-1} around the observed-frame [N II] frequency with a CASA task `immoments`, excluding channels at -139 to -61 km s^{-1} that are noisy through an atmospheric absorption. In the right panel of Figure 1, the contours illustrate the [N II] flux map. Figure 2 shows a spatially-integrated spectrum in a $1''$ -radius aperture around the galaxy. The noise spectrum shown by the dotted lines is measured by placing

Table 1. A summary of measurements of B14-65666.

Parameters	measurements	references
[N II] flux [Jy km s^{-1}]	< 0.0514	This study
[O III] flux [Jy km s^{-1}]	1.5 ± 0.18	H19
[C II] flux [Jy km s^{-1}]	0.87 ± 0.11	H19
[N II] luminosity [L_{\odot}]	$< 8.1 \times 10^7$	This study
[O III] luminosity [L_{\odot}]	$(3.4 \pm 0.4) \times 10^9$	H19
[C II] luminosity [L_{\odot}]	$(1.1 \pm 0.1) \times 10^9$	H19
90 μm flux density [μJy]	470 ± 128	H19
120 μm flux density [μJy]	218 ± 19	This study
160 μm flux density [μJy]	130 ± 25	H19

NOTE— The measurements taken from H19 represent total values, meaning the whole emission from two clumps.

References— H19: Hashimoto et al. (2019)

500 random apertures of the same radii. There is no significant detection with $S/N > 3$ in the image and spectrum.

An upper limit of the [N II] line emission is measured from the uncertainty of the flux map. The rms of the [N II] flux map is $17.1 \text{ mJy beam}^{-1}\text{km s}^{-1}$. Given the source size of the HST image, the galaxy will not be resolved spatially. Therefore, the 3σ upper limit of the [N II] flux is computed

from the rms in the flux map to be $51.4 \text{ mJy km s}^{-1}$, by adopting the spatial size of a single beam. The line flux limit is converted to the line luminosity limit using the luminosity distance and observed frequency (Carilli & Walter 2013). The [N II] line luminosity is constrained to be $8.1 \times 10^7 L_\odot$ as the 3σ upper limit. The [N II] line flux and luminosity are listed in Table 1, as well as the [O III] and [C II] lines taken from Hashimoto et al. (2019).

The constraint of [N II] line luminosity is lower than the measurements for star-forming/starburst galaxies in literature. Lee et al. (2019) detected an [N II] 122 μm line in BRI 1202-0725 SMG at $z = 4.96$ and obtained the line luminosity of $2.71 \pm 0.65 \times 10^9 L_\odot$. The [N II] line luminosity of SPT 0418-47 at $z = 4.2$ measured by De Breuck et al. (2019) is $1.6 \pm 0.5 \times 10^8 L_\odot$, which is corrected with the gravitational magnification factor of $\mu = 32.7$ (Spilker et al. 2016). Harikane et al. (2020) observed three LBGs at $z \sim 6$ with ALMA but did not detect the [N II] line for any of the three objects, while they did detect [O III] 88 μm and [C II] 158 μm lines. The [N II] luminosities of these objects are $< 6.2 \times 10^8$, $< 8.3 \times 10^8$, and $< 1.2 \times 10^9 L_\odot$ for the upper limits, which are integrated in 600 km s^{-1} velocity width and a $2''$ -radius aperture. Our upper limit of [N II] luminosity is several times lower than these constraints in literature despite the higher redshift of B14-65666.

4. FIR SED FITTING

4.1. Modified Blackbody Fitting

We perform FIR SED fitting to estimate the IR luminosity and dust mass by combining the new 120 μm dust continuum emission with previous measurements of 90 and 160 μm dust continua underlying [O III] 88 μm and [C II] 158 μm . In this paper, we only discuss the total FIR SED, assuming a constant dust temperature in the entire system of B14-65666, while the galaxy is composed of two components and suggested to be a merging system (Hashimoto et al. 2019). First, we fit a standard modified blackbody function to the observed FIR flux densities:

$$F_\nu^{\text{obs}} = \frac{1+z}{d_L^2} M_d \kappa_\nu \{B_\nu(T_d) - B_\nu(T_{\text{CMB}})\}, \quad (1)$$

where z is the source redshift, and d_L is the luminosity distance. M_d is the dust mass, which is the normalization of the equation. κ_ν is the dust emissivity at the frequency ν . $B_\nu(T)$ is the blackbody function, and T_d is the dust temperature of the source. T_{CMB} is the cosmic microwave background (CMB) temperature at the source redshift, and $B_\nu(T_{\text{CMB}})$ denotes CMB intensity. The negative $B_\nu(T_{\text{CMB}})$ term accounts for a correction of CMB effect in interferometric observations (da Cunha et al. 2013).

Although assumptions on the emissivity value systematically affect estimates of dust mass (e.g., Fanciullo et al. 2020), there are large varieties among empirical estimates, theoretical models, and laboratory measurements of emissivity, as briefly reviewed in Inoue et al. (2020). Following Inoue et al. (2020), we assume $\kappa_\nu = 30 \text{ cm}^2 \text{ g}^{-1} (100 \mu\text{m}/\lambda)^\beta$

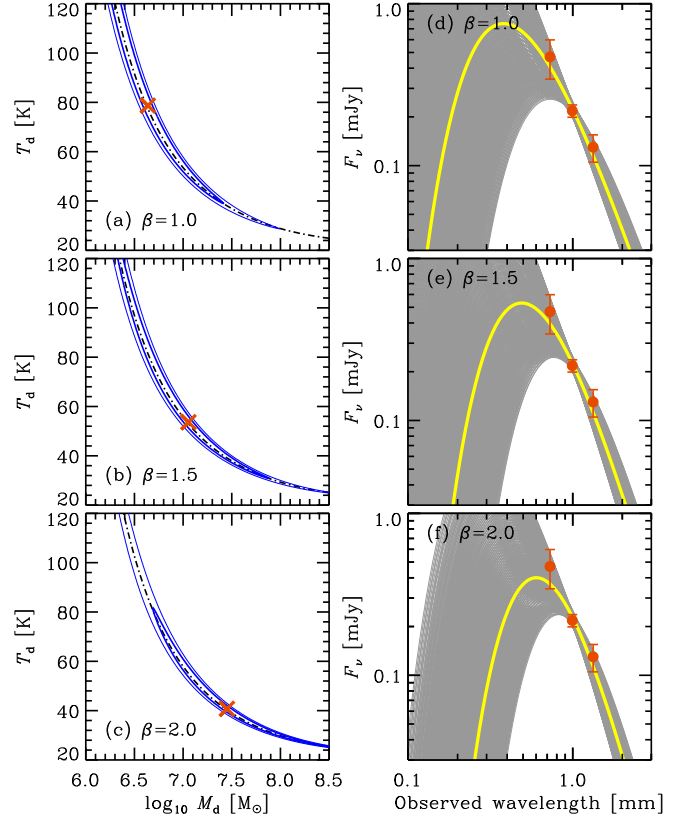


Figure 3. Modified blackbody fitting results. (a)–(c) The best-fit solutions (crosses) and central 68/95 percent (thick/thin solid lines) areas in the dust temperature and mass plane for the emissivity indices $\beta = 1.0, 1.5,$ and 2.0 . The dot-dashed lines show the sequences of dust temperature and mass that provide the observed Band 7 flux density. (d)–(f) FIR SEDs for best-fit solutions (thick yellow solid lines) and those in the 68 percent areas of the dust temperature–mass plane for $\beta = 1.0, 1.5,$ and 2.0 . The data points with error bars are the ALMA measurements.

with the wavelength $\lambda = c/\nu$ and the light speed c and the emissivity index $\beta = 1.0, 1.5,$ or 2.0 . Figure 3 shows the results obtained from the least- χ^2 fitting with two free parameters of M_d and T_d . There is a degeneracy between M_d and T_d because we do not constrain the peak of FIR SED yet. A data point at a shorter wavelength than 90 μm is important to break this degeneracy. The best-fit T_d spans 80 K to 40 K and is lower for a larger β . The best-fit $\log_{10}(M_d/M_\odot)$ increases from 6.6 to 7.5 with increasing β . The corresponding IR luminosity changes from $\log_{10}(L_{\text{IR}}/L_\odot) = 12.0$ to 11.6. The obtained values and their uncertainties are listed in appendix Table A1. Although we find a smallest χ^2 value for $\beta = 1.0$, χ^2 differences compared to $\beta = 1.5$ or 2.0 are not statistically significant.

4.2. Radiative Equilibrium Fitting

Inoue et al. (2020) presented a new algorithm to derive dust temperature and mass using radiative equilibrium on dust grains. Radiative equilibrium connects T_d with M_d and

breaks degeneracy between them. Therefore, we may obtain tighter constraints on them even without observing the FIR SED peak. The algorithm requires the observed UV luminosity, L_{UV} , and the physical radius of the system, R . We adopt values taken from Hashimoto et al. (2019). The total UV luminosity is $L_{UV} = (7.6 \pm 1.3) \times 10^{44} \text{ erg s}^{-1}$. The observed full-width half-maximum along the major and minor axes of the entire dust emission in Band 6 are $a = 3.8 \pm 1.1 \text{ kpc}$ and $b = 0.8 \pm 0.5 \text{ kpc}$ in the proper coordinate, respectively. The Band 6 observation in Hashimoto et al. has higher spatial resolution than our Band 7 observation. Assuming a spherical symmetric structure for the analytic treatment of Inoue et al. (2020), we adopt the radius of $R = \sqrt{ab}/2 = 0.87 \pm 0.30 \text{ kpc}$.

Following Inoue et al. (2020), we perform least- χ^2 fitting for FIR SED with the radiative equilibrium algorithm in three geometries: spherical shell, homogeneous sphere, and clumpy sphere. The spherical shell and homogeneous sphere geometries require only a single free parameter, M_d (or T_d), and the other quantity of T_d (or M_d) is derived from M_d (or T_d) thanks to the radiative equilibrium. The clumpy geometry requires an additional free parameter to control the clumpiness, ξ_{cl} , which is a non-dimensional parameter defined by the ratio between a single clump size relative to the entire system size and the volume filling factor of the clumps. Figure 4 shows the fitting results for the case of $\beta = 2.0$. The other two β cases are shown in appendix Figure 11. Radiative equilibrium requires the relations between T_d and M_d shown by the short-dashed, long-dashed, and dotted lines for the shell, homogeneous, and clumpy geometries, respectively. We consider the uncertainties of L_{UV} and R in addition to FIR flux densities in the fitting using a Monte Carlo method (Inoue et al. 2020). Therefore, the resultant uncertainties in M_d and T_d are still large. The clumpy geometry case gives the same best-fit solutions as those of the modified blackbody fitting because the clumpiness parameter functions as an adjuster (Inoue et al. 2020). Figure 5 shows the best-fit FIR SEDs for $\beta = 2.0$ and Figure 6 shows the distribution of the solutions in the M_d and ξ_{cl} plane for $\beta = 2.0$. Other β cases are found in Figures 12 and 13, respectively. The numerical values are summarized in appendix Table A1. For the shell and homogeneous geometries, the cases of $\beta = 1.5$ and 2.0 result in larger χ^2 values and are not favored statistically compared to the case of $\beta = 1.0$. For the clumpy geometry, all β cases cannot be different statistically.

The best-fit T_d values are $\simeq 100 \text{ K}$ in the shell geometry, 80–100 K in the homogeneous geometry, and 40–80 K in the clumpy geometry. The corresponding $\log_{10}(M_d/M_\odot)$ values are 6.4–6.6, 6.5–6.7, and 6.6–7.5, respectively. The IR luminosities are $\log_{10}(L_{IR}/L_\odot) = 12.5\text{--}13.0$, 12.4–12.6, and 11.6–12.1, respectively. Comparing our results for B14-65666 to those for another $z \simeq 7$ DSFG, A1689zD1, discussed in Inoue et al. (2020), we find some similarities in the dust properties of those high-redshift objects. In the shell and homogeneous geometries, both objects exhibit high IR luminosities and corresponding high SFRs, possibly indicating the invalidity of these simple geometries. In the clumpy

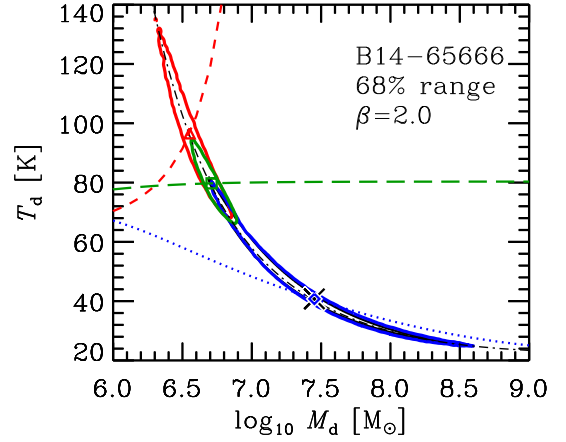


Figure 4. Best-fit solutions (symbols) and 68 percent areas (solid lines) in the radiative equilibrium fitting, and the dust temperature and mass plane for the emissivity index $\beta = 2.0$. The red triangle, green square, and blue diamond represent the best-fit solutions in the shell, homogeneous, and clumpy geometries, respectively. The black cross represent the best-fit solution in the modified blackbody case. The dot-dashed line shows the dust temperature–mass relation of the observed Band 7 flux density. The red short-dashed, green long-dashed, and blue dotted lines show the dust temperature–mass relations in the radiative equilibrium for the shell, homogeneous, and clumpy models, respectively.

geometry, the best-fit clumpiness parameter is $\xi_{cl} = 0.1\text{--}0.4$ for B14-65666, which is similar to that for A1689zD1. As discussed in Inoue et al. (2020), if a clump size is similar to the size of giant molecular clouds of $\sim 10 \text{ pc}$ in the local Universe (Larson 1981; Fukui et al. 2008), these values correspond to a clump volume filling factor of 3%–10%. Although observing such tiny clouds are difficult without significant gravitational lensing, a comparison between the clumpiness expected from the radiative equilibrium algorithm and galaxy formation simulations will be interesting.

5. DISCUSSION

5.1. Ratio of [N II] to IR luminosity

In the following, we adopt the case of the clumpy geometry at $\beta = 2.0$ for the IR luminosity. In Figure 7, we compare the ratio of the [N II] 122 μm to IR luminosity ($L_{[\text{N II}]122}/L_{\text{IR}}$) with the ratios in the literature. The observed line-to-IR luminosity ratio decreases with increasing IR luminosity in local luminous infrared galaxies (line deficit; e.g., Herrera-Camus et al. 2018a,b). Figure 7 shows $L_{[\text{N II}]122}/L_{\text{IR}}$ as a function of L_{IR} . The three red circles show the measurements of this study, reflecting the uncertainties of the IR luminosity in the clumpy geometry. The gray open symbols depict the local reference measurements: dwarf galaxies (Madden et al. 2013; Cormier et al. 2015), ultra/luminous infrared galaxies (Farrah et al. 2013), and star-forming, Seyfert, and luminous infrared galaxies (Herrera-Camus et al. 2018b). The $L_{[\text{N II}]122}/L_{\text{IR}}$ upper limits of B14-65666 is on the relation of

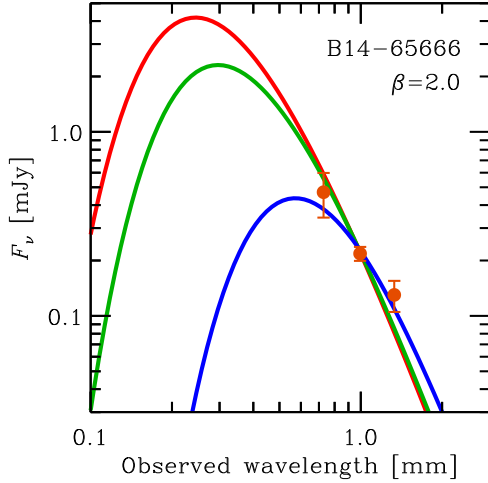


Figure 5. Best-fit FIR SEDs for the shell (red), homogeneous (green), and clumpy (blue) models. The data points with error bars are ALMA measurements. The emissivity index is $\beta = 2.0$.

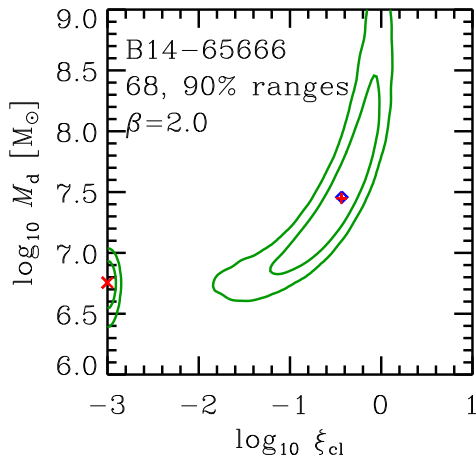


Figure 6. Distribution of the best-fit solutions obtained from 30,000 Monte Carlo trials for perturbed observational data in the clumpy model for the emissivity index $\beta = 2.0$. The vertical and horizontal axes are dust mass and the clumpiness parameter, respectively. The contours enclose 68 percent and 90 percent of the solutions. The diamond shows the best-fit solution for the actual observational data. The plus sign and cross symbol represent the highest and second highest peaks of the density of the solutions, respectively.

the local galaxies. At high redshift, SPT 0418-47 exhibits an [N II] luminosity consistent with the local galaxies (De Breuck et al. 2019). In contrast, some high-redshift objects are located above the local relations, like BRI 1202-0725 SMG (Iono et al. 2006; Lee et al. 2019) and $z > 4$ quasars (Novak et al. 2019; Lee et al. 2019; Li et al. 2020) as discussed in Li et al. (2020). Our analysis demonstrates that

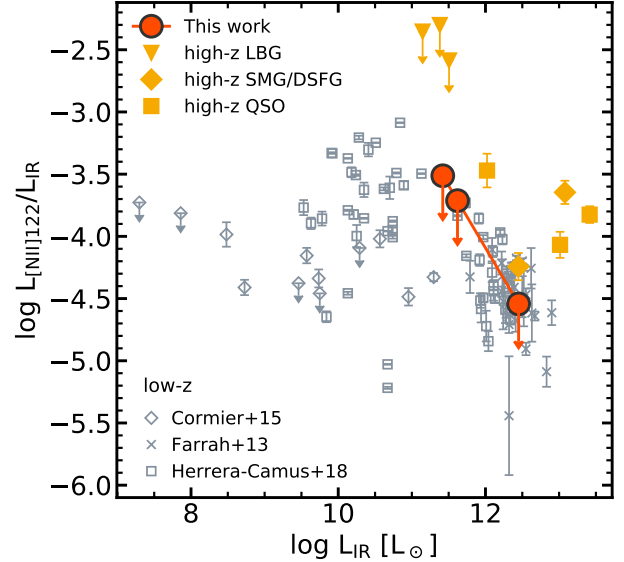


Figure 7. The ratio of [NII] 122 μm to the IR luminosity as a function of the IR luminosity. The red circles represent the constraints for B14-65666. The left and right circles reflect the errors of the IR luminosity estimated with the radiative equilibrium fitting assuming the clumpy geometry at $\beta = 2.0$. The orange filled symbols show the measurements for high-redshift objects: three LBGs at $z \sim 6$ (upside-down triangles, Harikane et al. 2020), SMG/DSFG at $z = 4-5$ (diamonds, Lee et al. 2019; De Breuck et al. 2019), and $z > 4$ quasars (squares, Novak et al. 2019; Lee et al. 2019; Li et al. 2020). The gray open symbols are taken from studies on local galaxies: Cormier et al. (2015, diamonds), Farrah et al. (2013, crosses), and Herrera-Camus et al. (2018b, squares). In this figure, the error bars of the references only include the errors of the [N II] luminosity. The upper limits for B14-65666 are located in the distribution of the local galaxies and do not show any excess as some of the high-redshift objects.

B14-65666 does not show an excess in the [N II]-to-IR luminosity ratio from the local decreasing trend.

5.2. Estimates of Nebular Physical Parameters

Emission-line ratios originating from star-forming activities are determined by physical properties of nebulae around massive stars. Given nebular parameters and ionizing radiation sources, photoionization models of the nebulae can be constructed, and the emission-line fluxes from various atoms and ions can be predicted. In this section, we use a photoionization code Cloudy (Ferland et al. 1998) to examine principal nebular parameters, i.e., the metallicity Z , ionization parameter U , and hydrogen density n_{H} at a surface illuminated by an ionizing radiation source.

The luminosities of [O III] 88 μm ($L_{[\text{OIII}88]}$) and [C II] 158 μm ($L_{[\text{CII}158]}$) lines provide information on the nebular parameters. We use the $L_{[\text{OIII}88]}/\text{SFR} - L_{[\text{CII}158]}/\text{SFR}$ diagram proposed by Harikane et al. (2020) to estimate the nebular pa-

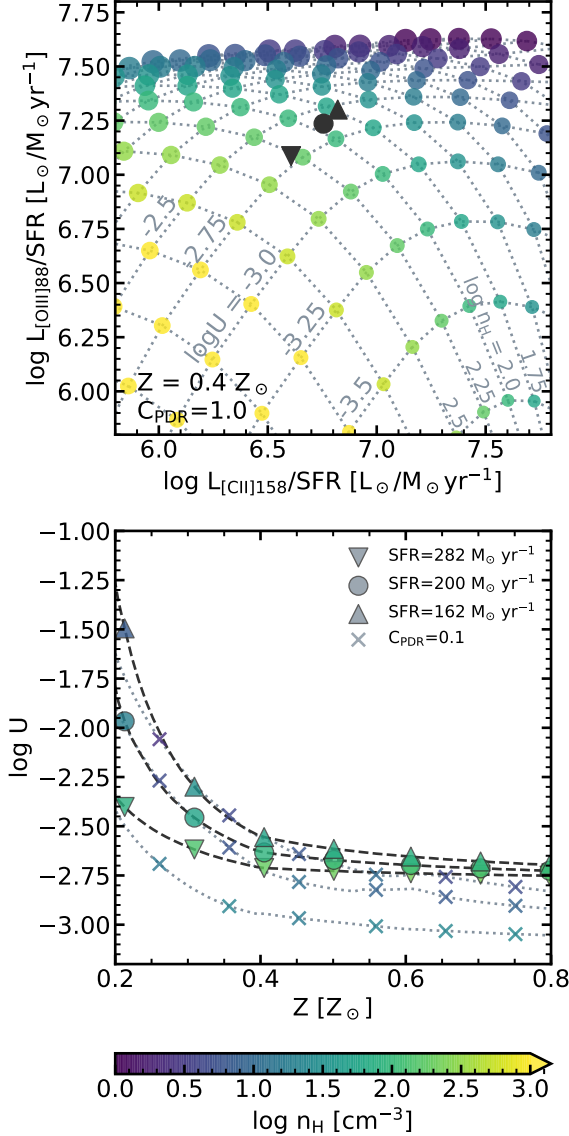


Figure 8. Top: $L_{[\text{OIII}]88}/\text{SFR}$ – $L_{[\text{CII}]158}/\text{SFR}$ diagram. The grid shows the result of the Cloudy model at the metallicity of $0.4 Z_{\odot}$, where the circle sizes and colors depend on the ionization parameter U and hydrogen density n_{H} , respectively. The ranges of parameters are $-4.0 < \log_{10} U < -0.5$ and $0 < \log_{10} n_{\text{H}}/\text{cm}^{-3} < 4.0$ in steps of 0.25. The black symbols show the location of B14-65666 on the diagram. The triangle, circle, and upside-down triangle show the SFR differences of 162, 200, and $282 M_{\odot} \text{ yr}^{-1}$, respectively. Bottom: Ionization parameter U as a function of the metallicity Z color-coded by hydrogen density n_{H} . The three dashed sequences represent the differences of the SFR. The dotted lines with the crosses represent the case of $C_{\text{PDR}} = 0.1$. At $Z > 0.4 Z_{\odot}$ U is almost constant at $\log_{10} U \simeq -2.7 \pm 0.1$ and n_{H} is $50\text{--}250 \text{ cm}^{-3}$, whereas at $Z < 0.4 Z_{\odot}$ both nebular parameters drastically change.

rameters. Harikane et al. illustrated a diagram that compared $L_{[\text{OIII}]88}/\text{SFR}$ and $L_{[\text{CII}]158}/\text{SFR}$ as functions of U , n_{H} , Z , and other parameters. We adopt the concepts of Harikane et al. and Nagao et al. (2011, 2012) to model H II regions and PDRs in a plain-parallel geometry using a software Cloudy version 17.01 (Ferland et al. 2017) under the assumptions of the pressure equilibrium, an identical metallicity in the stellar and gas phases, and the solar C/O abundance. The software is run until the V-band dust extinction reaches 100 mag (Abel et al. 2005). Following Inoue et al. (2014), in our model, we use the input spectra of 10-Myr constant star-formation models at stellar metallicities of $Z_{*} = 0.02, 0.2, 0.4$, and $1.0 Z_{\odot}$, created with the STARBURST99 (Leitherer et al. 1999) with a Salpeter initial mass function at $1\text{--}100 M_{\odot}$. We also test input spectra created with the Binary Population and Spectral Synthesis code (BPASS, Eldridge et al. 2017) version 2.2.1 (Stanway & Eldridge 2018) to find that the results are qualitatively the same and that our conclusions do not change. The remaining free parameters are U , n_{H} , Z , and the PDR covering fraction C_{PDR} . We perform Cloudy modeling with $-4.0 < \log_{10} U < -0.5$ and $0 < \log_{10} n_{\text{H}}/\text{cm}^{-3} < 4.0$ in steps of 0.25. SFR is converted from the modeled $\text{H}\alpha$ line flux with Equation 2 in Kennicutt (1998) by multiplying it with a conversion factor of 0.63 (Madau & Dickinson 2014) from Salpeter (1955) to Chabrier (2003) initial mass functions, in order to use the same initial mass function as used for the observed SED SFR. If Z and C_{PDR} are fixed, a nebular parameter pair (U , n_{H}) is in one-to-one correspondence to ($L_{[\text{OIII}]88}/\text{SFR}$, $L_{[\text{CII}]158}/\text{SFR}$), as shown in the top panel of Figure 8. Here, we derive U and n_{H} as functions of Z by using $C_{\text{PDR}} = 1.0$ and 0.1 as fiducial parameters.

The SFR and gas-phase metallicity of B14-65666 are almost constrained to be $\text{SFR} = 200_{-38}^{+82} M_{\odot} \text{ yr}^{-1}$ and $Z = 0.4_{-0.2}^{+0.4} Z_{\odot}$ using SED fitting in Hashimoto et al. (2019). SED fitting uses photometry from NIR to ALMA FIR bands (from UV to FIR bands in the rest frame), including the effect of dust attenuation. The estimated metallicity is consistent with another estimated metallicity from the $[\text{O III}] 88 \mu\text{m}$ luminosity and SFR by Jones et al. (2020). Compared to the errors of $\simeq 12\%$ in $L_{[\text{OIII}]88}$ and $L_{[\text{CII}]158}$, the SFR error is large and dominates measurement uncertainties in the results. We, therefore, evaluate uncertainties in the nebular parameters using $\text{SFR} = 162, 200$, and $282 M_{\odot} \text{ yr}^{-1}$ at metallicities from $Z = 0.2$ to $0.8 Z_{\odot}$. At each metallicity, ($L_{[\text{OIII}]88}/\text{SFR}$, $L_{[\text{CII}]158}/\text{SFR}$) values can be converted into (U , n_{H}) values through linear interpolation. Figure 8 displays the $L_{[\text{OIII}]88}/\text{SFR}$ – $L_{[\text{CII}]158}/\text{SFR}$ diagram at $Z = 0.4 Z_{\odot}$ and $C_{\text{PDR}} = 1.0$ in the top panel. The model grid in the diagram depends on the Z and C_{PDR} values. The modeled $[\text{O III}]$ values increase with an increase in metallicity due to high oxygen abundances, whereas the modeled $[\text{C II}]$ values decrease with a decrease in C_{PDR} by almost the same factor. We refer readers to Harikane et al. (2020) for detailed characteristics of the models.

The bottom panel of Figure 8 shows the estimated U values as a function of Z , color-coded by n_{H} . The triangles, circles, and upside-down triangles show the low (162), middle (200),

and high ($282 M_{\odot} \text{ yr}^{-1}$) SFR cases for $C_{\text{PDR}} = 1.0$, respectively. Both U and n_{H} monotonically decreases and increases at a fixed SFR, respectively, as the assumed metallicity increases. At high metallicities of $Z > 0.4 Z_{\odot}$, the ionization parameter is almost constant at $\log_{10} U \simeq -2.7 \pm 0.1$ and the hydrogen density is $n_{\text{H}} \simeq 50\text{--}250 \text{ cm}^{-3}$. The dispersion of U caused by SFR uncertainty is small. The U values are comparable with those in local dwarf (Cormier et al. 2019) and $z \sim 2$ galaxies (Strom et al. 2018) in similar metallicity range, as well as nearby starburst galaxies with higher metallicity (Herrera-Camus et al. 2018a). Specifically, these U values are on U - Z invariant relation from local to $z \sim 2$ galaxies (Sanders et al. 2020). The range of the hydrogen density of our galaxy is between the average values of that of local and $z \sim 2$ galaxies (Sanders et al. 2016). We do not find any further increase of hydrogen density from $z \sim 2$ to 7 even though hydrogen density increases with an increase in redshift by a factor of 10 from $z \sim 0$ to 2 galaxies (e.g., Sanders et al. 2016). In contrast, at $Z < 0.4 Z_{\odot}$, $\log_{10} U$ drastically increases up to -1.0 with a decrease in metallicity. Hydrogen density simultaneously drops to $n_{\text{H}} \sim 1 \text{ cm}^{-3}$. Such extreme conditions of the nebular parameters are hardly found in normal galaxies at low redshifts, whereas dwarf galaxies with low metallicity and low specific SFR tend to exhibit similar high U and low n_{H} (Cormier et al. 2019). These drastic changes in the nebular parameters are caused by the high B14-65666 $L_{[\text{O III}]88}/\text{SFR}$ ratio, which is difficult to explain in low metallicity regimes in our model. Notably, our model cannot reproduce the observed high $L_{[\text{O III}]88}/\text{SFR}$ ratio at $Z < 0.1 Z_{\odot}$ even in the high SFR case. The crosses in Figure 8 depict the models at $C_{\text{PDR}} = 0.1$. In this case, U and n_{H} become smaller than the $C_{\text{PDR}} = 1.0$ case at a fixed metallicity. Specifically, n_{H} is predicted to be low; the values are smaller by an order of magnitude at $Z > 0.4 Z_{\odot}$ and $n_{\text{H}} \lesssim 10 \text{ cm}^{-3}$ at $Z < 0.4 Z_{\odot}$. However, qualitative tendencies of U and n_{H} to Z are unaffected by C_{PDR} difference.

Although we assume that [C II] is emitted from H II regions and PDRs, [C II] emission also arises from shock excitation caused by galaxy interactions. It can be a cause for concern that shocks contribute to the [C II] line flux since B14-65666 exhibits a merger morphology (Hashimoto et al. 2019). Appleton et al. (2013) measured the [C II] flux originating from shocks by observing the intergalactic medium in Stephan’s Quintet. They report that the [C II]-to-IR luminosity ratios are $> 10^{-1.5}$, which is higher than those measured in star-forming galaxies, including B14-65666 ($\sim 10^{-2.5}$, Hashimoto et al. 2019). The [C II] luminosity by shocks ($\sim 10^7 L_{\odot}$) is also lower than for B14-65666 ($\sim 10^9 L_{\odot}$). We, therefore, conclude that shock excitation is less dominant in [C II] emission in B14-65666 unless the shock mechanism significantly differs between two objects.

5.3. Nitrogen-to-Oxygen Abundance Ratio

As seen in dwarf galaxies (e.g., Lequeux et al. 1979; Vila-Costas & Edmunds 1993) and SDSS galaxies (Andrews & Martini 2013), the N/O abundance ratio is almost constant as $\log_{10}(\text{N/O}) \simeq -1.5$ at low metallicity, and it drastically

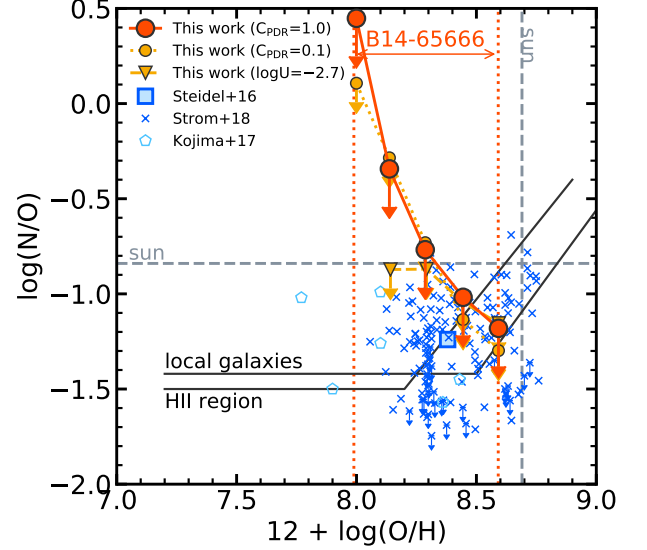


Figure 9. The nitrogen-to-oxygen abundance ratio as a function of metallicity. The red circles show the upper limits of B14-65666 at $C_{\text{PDR}} = 1.0$ and $12 + \log_{10}(\text{O}/\text{H}) = 7.97\text{--}8.57$, corresponding to $Z = 0.2\text{--}0.8 Z_{\odot}$ (red line). The small orange circles show the case of $C_{\text{PDR}} = 0.1$. The orange upside-down triangles show the case in which the ionization parameter is fixed at $U = -2.7$. The black solid lines show the average relations of extragalactic HII regions (Pilyugin et al. 2012) and local SDSS galaxies (Andrews & Martini 2013) estimated using the direct temperature method. The blue and cyan data points show the $z \sim 2$ galaxies without error bars: Strom et al. (2018, blue crosses), Steidel et al. (2016, blue square), and Kojima et al. (2017, cyan pentagon). The gray dashed lines indicate the solar values. The N/O ratio is constrained to be sub-solar at $12 + \log_{10}(\text{O}/\text{H}) \gtrsim 8.4$.

increases when metallicity exceeds a certain value. A simple explanation of this N/O trend is a combination of the primary and secondary nucleosynthetic nitrogen; the primary production of nitrogen is independent of the initial metallicities in stars, whereas the secondary production that occurred in the CNO cycle is proportional to the initial carbon or oxygen abundance (Pagel 2009). The N/O ratio affects the intensity ratios between nitrogen and oxygen atoms/ions emission lines. Given the nebular parameters and input spectrum (i.e., a certain fixed ionization structure), photoionization models can predict abundance ratios from observed emission-line intensity ratios. Therefore, if we assume the nebular parameters derived from the line ratio of [O III] to [C II], the N/O abundance ratio at $z \sim 7$ can be constrained by our upper limits of the luminosity ratio between [N II] 122 μm and [O III] 88 μm ($L_{[\text{N II}]122}/L_{[\text{O III}]88}$).

We convert $L_{[\text{N II}]122}/L_{[\text{O III}]88}$ to N/O with a set of Cloudy models using the nebular parameters obtained in Section 5.2, which are functions of metallicity (see Figure 8). For each nebular parameter set (i.e., each metallicity), we prepare

models with $\log_{10}(\text{N/O})$ ranging from -2 to 0 in steps of 0.5 . We note that n_{H} is included in our calculations even though $L_{[\text{NII}]122}/L_{[\text{OIII}]88}$ is almost independent of n_{H} due to similar critical densities between $[\text{NII}] 122 \mu\text{m}$ and $[\text{OIII}] 88 \mu\text{m}$. We obtain the upper limits of N/O as a function of U and Z by comparing $L_{[\text{NII}]122}/L_{[\text{OIII}]88}$ ratios in our observation and the Cloudy models. At a fixed Z , higher U results in a higher N/O upper limit (i.e., a weaker N/O constraint). To simply express N/O as a function of Z , we take the highest N/O ratios as the upper limits at each Z .

Figure 9 illustrates the N/O abundance ratio of B14-65666 as a function of metallicity. Given that the solar value of $12 + \log_{10}(\text{O/H})$ is 8.69 (Asplund et al. 2009), the metallicity Z is converted to the O/H abundance ratio. The N/O value is well constrained at a high metallicity regime. This originates from a model prediction of relatively high $L_{[\text{NII}]122}/L_{[\text{OIII}]88}$ for the range of ionization parameters at high metallicities. At $12 + \log_{10}(\text{O/H}) \gtrsim 8.4$, $\log_{10}(\text{N/O})$ is less than the solar value of -0.84 (Asplund et al. 2009). At a higher metallicity of $12 + \log_{10}(\text{O/H}) > 8.5$, the $\log_{10}(\text{N/O})$ upper limits become less than the average relation of extragalactic H II regions (Pilyugin et al. 2012). On the other hand, the N/O constraint is very weak at $12 + \log_{10}(\text{O/H}) < 8.3$ due to high ionization parameters of $\log U \gtrsim -2.5$. If the metallicity of B14-65666 is $12 + \log_{10}(\text{O/H}) < 8.3$, our observations cannot produce a meaningful constraint on the N/O abundance, implying that we need more sensitive observations by 1–2 order of magnitude to detect the $[\text{N II}] 122 \mu\text{m}$ emission line from the $z \sim 7$ galaxy. The small orange circles in Figure 9 depict the case of $C_{\text{PDR}} = 0.1$. We find that the low PDR covering fraction only weakly affects the upper limits of the N/O ratio by 0.1-dex at most even though it decreases the upper limit by 0.4 dex only at $12 + \log_{10}(\text{O/H}) = 8.0$. As shown in Figure 8, the low C_{PDR} weakly changes U in the low SFR case, which influences the N/O upper limit. Although n_{H} decreases in this case, $L_{[\text{NII}]122}/L_{[\text{OIII}]88}$ is almost independent of n_{H} and the N/O constraints are not affected. Therefore, the lower C_{PDR} does not change the N/O abundance very much.

The weak N/O upper limits at $12 + \log_{10}(\text{O/H}) < 8.3$ originates from the high ionization parameters of $\log_{10} U \gtrsim -2.5$. If the ionization parameter of B14-65666 is similar to those of local and $z \sim 2$ galaxies, the upper limits would become more stringent. We check this possibility by fixing $\log_{10} U = -2.7$ and by changing C_{PDR} on the $L_{[\text{OIII}]88}/\text{SFR} - L_{[\text{NII}]158}/\text{SFR}$ plane. In this analysis we choose nebular parameter sets that can model the observed value within the SFR uncertainty of $162 < \text{SFR} < 282 M_{\odot} \text{yr}^{-1}$ and take the highest N/O in the parameter sets as the upper limits at fixed metallicities. The results are depicted with the orange upside-down triangles in Figure 8. The assumption of $\log_{10} U = -2.7$ gives similar upper limits to the $C_{\text{PDR}} = 1.0$ case (red circles) at $12 + \log_{10}(\text{O/H}) > 8.3$. At lower metallicities of $12 + \log_{10}(\text{O/H}) < 8.3$, however, the upper limit is constant at $\log_{10}(\text{N/O}) = -0.87$, which is 3 times lower than the upper-limit values shown with the red and orange circles. This result demonstrates our explana-

tion that the weak N/O upper limits originates from the high ionization parameters. If $\log_{10} U = -2.7$, the N/O ratio of this galaxy is restricted to be sub-solar, irrespective of its intrinsic metallicity. In our model, low PDR covering fraction ($C_{\text{PDR}} < 1$) and high SFR ($282 M_{\odot} \text{yr}^{-1}$) are required to achieve $\log_{10} U = -2.7$ at lower metallicities. We note that we cannot plot the data point at $12 + \log_{10}(\text{O/H}) = 8.0$ in the figure because there are no models with $\log_{10} U = -2.7$ at this metallicity within the SFR uncertainty interval.

Our N/O upper limit is roughly consistent with $z \sim 2$ studies. Steidel et al. (2016) stacked the KBSS-MOSFIRE spectra to compute the typical N/O of them and Strom et al. (2018) estimated N/O for individual KBSS-MOSFIRE galaxies with photoionization models. These N/O ratios are comparable to those of the local extragalactic H II regions presented by Pilyugin et al. (2012). The relatively low metallicity galaxies at $z \sim 2$ studied by Kojima et al. (2017) exhibit higher $\log_{10}(\text{N/O})$ than local galaxies at fixed metallicities, which are measured using a direct temperature method. Most of these N/O ratios at $z \sim 2$ are lower than the upper limit of B14-65666. Our upper limits are also consistent with the nearby analogs of LBGs in Loaiza-Agudelo et al. (2020).

5.4. Predicted BPT Diagram

As noted in the previous section, the photoionization model can convert an emission-line flux into another line flux for the same ion. This enables us to predict the position of B14-65666 on the BPT diagram from our FIR line fluxes. We estimate optical-line ratios of $[\text{O III}]\lambda 5007/\text{H}\beta$ and $[\text{N II}]\lambda 6583/\text{H}\beta$ from the FIR $[\text{O III}] 88 \mu\text{m}$ and $[\text{N II}] 122 \mu\text{m}$ line fluxes, respectively, using the Cloudy models with the nebular parameters obtained in Section 5.2. In this model, $[\text{N II}]\lambda 6583/\text{H}\beta$ is given as an upper limit because the $[\text{N II}] 122 \mu\text{m}$ flux is constrained as the 3σ upper limit in our observations. The $\text{H}\alpha/\text{H}\beta$ line ratio is also computed from the model. In this way, we obtain the modeled $[\text{O III}]\lambda 5007/\text{H}\beta$ and $[\text{N II}]\lambda 6583/\text{H}\alpha$ line ratios for B14-65666.

Figure 10 plots a BPT diagram. In general, dust attenuation is negligible on the BPT diagram because the diagram takes the ratios of the emission lines with close wavelengths. The FIR $[\text{O III}] 88 \mu\text{m}$ and $[\text{N II}] 122 \mu\text{m}$ fluxes are not affected by dust attenuation due to their long wavelengths. For these reasons, our estimations can be compared with values in literature without concerns about dust attenuation.

The estimated optical-line ratios for B14-65666 are $\log_{10}([\text{O III}]/\text{H}\beta) = 0.55 \pm 0.02$ and $\log_{10}([\text{N II}]/\text{H}\alpha) < -0.71$ at $Z = 0.4 Z_{\odot}$. The $[\text{O III}]/\text{H}\beta$ ratios become high at $Z = 0.2 Z_{\odot}$ and low at $Z = 0.8 Z_{\odot}$, while both $[\text{N II}]/\text{H}\alpha$ upper limits become lower than the value at $Z = 0.4 Z_{\odot}$. These values are depicted with the red circles in Figure 10. We note that B14-65666 is located in the region where star-forming galaxies are distributed on the BPT diagram (Kauffmann et al. 2003), which is a natural consequence of including the starbursting spectrum into the Cloudy model calculations (Sec 5.2). We are assuming that the entire emission-line fluxes originate from star formation not from AGNs. When

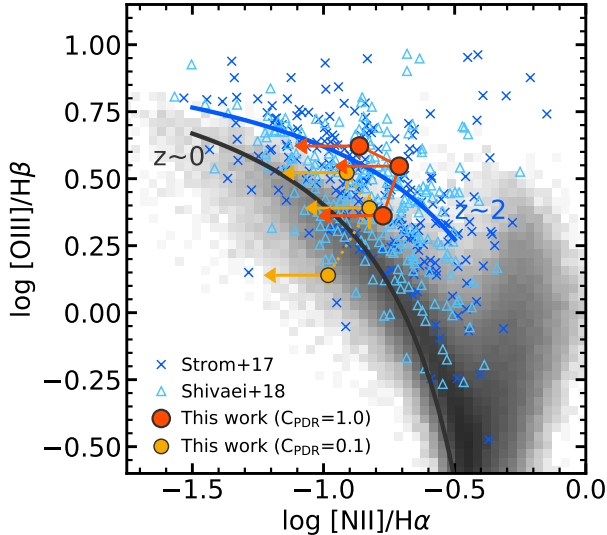


Figure 10. Estimated location of the B14-65666 upper limits on the BPT diagram. The location is computed from the photoionization model with the nebular parameters U , n , and Z (see the text in Section 5.4). The red circles are assumed as $C_{\text{PDR}} = 1.0$ and $Z = 0.2, 0.4$, and $0.8 Z_{\odot}$, where low metallicity data points show high $[\text{O III}]/\text{H}\beta$. The orange small circles denote the locations in the case of $C_{\text{PDR}} = 0.1$. The black density map indicates local SDSS galaxies. The blue crosses and cyan triangles indicate star-forming galaxies at $z \sim 2$ from the KBSS-MOSFIRE survey (Strom et al. 2017) and the MOSDEF survey (Shivaei et al. 2018), respectively. The black and blue lines represent the best-fit relations for the $z \sim 0$ SDSS galaxies and the $z \sim 2$ KBSS-MOSFIRE galaxies, respectively (Strom et al. 2017). As seen, B14-65666 is expected to be located on or below the $z \sim 2$ relation.

$C_{\text{PDR}} = 0.1$, the data points shown by the small orange circles move to the lower left, reflecting the low ionization parameter and hydrogen density.

To compare our results with low-redshift galaxies, we plot the distributions of local SDSS and $z \sim 2$ star-forming galaxies in Figure 10. The flux ratios of SDSS galaxies are taken from the MPA/JHU catalog³. The $z \sim 2$ galaxies are taken from the KBSS-MOSFIRE survey (Strom et al. 2017) and the MOSDEF survey (Shivaei et al. 2018). Our upper limits shown with the red circles ($C_{\text{PDR}} = 1.0$) are located above the local average relation and around the $z \sim 2$ relation (Strom et al. 2017). It is quite possible that B14-65666 is located below the average relation of the $z \sim 2$ galaxies even though our model provides only upper limits, considering the weak [N II] 122 μm flux suggested from the N/O upper limits at $Z < 0.4 Z_{\odot}$ (Figure 9). In the case of $C_{\text{PDR}} = 0.1$ (small orange circles), the upper limits are located around the $z \sim 0$ galaxies. At $Z = 0.8 Z_{\odot}$ in this case, especially

low $[\text{N II}]/\text{H}\alpha$ and $[\text{O III}]/\text{H}\beta$ values are predicted because the [N II] 122 μm line was undetected despite the low metallicity and low ionization parameters. In summary, our model predicts that B14-65666, at $z \sim 7$, is located on or below the average relation at $z \sim 2$ on the BPT diagram. If C_{PDR} is low, the location will become close to the $z \sim 0$ relation.

If B14-65666 is representative of the entire galaxy population at $z \sim 7$, we can discuss the redshift evolution from $z \sim 7$ to 2 on the BPT diagram by comparing the location of B14-65666 with the $z \sim 2$ relation. However, the large dispersions of the galaxy distributions on the BPT diagram at $z \sim 0$ and 2 raise a possibility that B14-65666 is not on the average relation at $z \sim 7$. In addition, the high UV luminosity and merger geometry of B14-65666 may not support the assumption that this galaxy is representative of the typical galaxies at $z \sim 7$. Further ALMA observations will explore the average ionization properties and distribution on the BPT diagram of the high-redshift galaxies. More directly, the upcoming JWST will provide us opportunities to plot the BPT diagram at high-redshift by observing B14-65666 and other high-redshift galaxies in near- to mid-infrared bands.

6. SUMMARY

We have performed ALMA Band 7 observations of a LBG at $z = 7.15$, B14-65666, to target the [N II] 122 μm FIR fine-structure line and underlying dust continuum emission. B14-65666 is the first object detected in [O III] 88 μm , [C II] 158 μm , and dust continuum emission at such high-redshift (“Big Three Dragons”, Hashimoto et al. 2019).

The dust continuum at 120 μm is detected with $S/N = 18.9$. We combine the dust-continuum flux at 120 μm with the previous measurements at 90 μm and 160 μm to perform two types of FIR SED fitting. The modified blackbody fitting results in a dust temperature $T_d = 80$ to 40 K and a dust mass $M_d \sim 10^{6.6}$ to $10^{7.5} M_{\odot}$ with an emissivity index $\beta = 1$ to 2. The corresponding IR luminosity spans $\log_{10}(L_{\text{IR}}/L_{\odot}) = 12.0$ to 11.6. The results of the radiative equilibrium fitting, proposed by Inoue et al. (2020), are found to be similar to the results for another $z \simeq 7$ dusty star-forming galaxy, A1689zD1. Simple assumptions of the shell and homogeneous geometries appear to be invalid because the geometries prefer too high IR luminosity. The clumpy geometry leads to the same best-fit results as the modified blackbody, with a best-fit clumpiness parameter of $\xi_{\text{cl}} = 0.1$ –0.4.

The [N II] 122 μm emission line is not detected. The 3σ upper limit of [N II] luminosity is $8.1 \times 10^7 L_{\odot}$. We constrain the nebular parameters of B14-65666 as functions of metallicity with a photoionization code Cloudy, by modeling the [N II] 122 μm upper limits, along with the [O III] 88 μm and [C II] 158 μm line fluxes and the SED SFR. If the metallicity of B14-65666 is high ($Z > 0.4 Z_{\odot}$), the ionization parameters and hydrogen densities are $\log_{10} U \simeq -2.7 \pm 0.1$ and $n_{\text{H}} \simeq 50$ –250 cm^{-3} , respectively. The two nebular parameter values are consistent with those measured in low-redshift galaxies. If $Z < 0.4 Z_{\odot}$, the U and n drastically increase and decrease, respectively, with a decrease in metal-

³ URL: <https://wwwmpa.mpa-garching.mpg.de/SDSS/DR7/>

licity. This is due to the observed high $L_{\text{[OIII]88}}/\text{SFR}$ ratio of this galaxy. In the case of a low PDR covering fraction ($C_{\text{PDR}} = 0.1$), lower U and n_{H} are expected, while the results are qualitatively the same.

The constraints on the nitrogen-to-oxygen abundance ratio, N/O, also largely depend on the assumed metallicity. The obtained upper limit of the N/O ratio monotonically decreases as the assumed metallicity increases. At $12 + \log_{10}(\text{O}/\text{H}) \gtrsim 8.4$, the N/O ratios could be sub-solar and upper limits are comparable to the N/O ratio of local and $z \sim 2$ galaxies. In contrast, our observations cannot provide meaningful constraint at $12 + \log_{10}(\text{O}/\text{H}) < 8.3$. The N/O ratio is insignificantly affected by the differences of the PDR covering fractions between $C_{\text{PDR}} = 0.1$ and 1.0. If we fix the ionization parameter at $\log U = -2.7$ in our model, the N/O ratios are restricted to be sub-solar even at $12 + \log_{10}(\text{O}/\text{H}) < 8.3$ with a small PDR covering fraction and a high SFR.

The Cloudy models also predict the location of the galaxy at $z \sim 7$ on the BPT diagram, using the nebular parameters estimated from the FIR lines. The upper limits of B14-65666 are predicted to be located in the distribution of star-forming galaxies at $z \sim 2$. The location of B14-65666 may be below the $z \sim 2$ average relation given the weak N/O upper limits. In the case of $C_{\text{PDR}} = 0.1$, the upper limits are located around the distribution of local galaxies. Further ALMA statistical observations and rest-frame optical-line observa-

tions with JWST will provide opportunities for addressing the high-redshift BPT diagram.

ACKNOWLEDGMENTS

We acknowledge Yuichi Harikane for providing us with the Cloudy data. We thank Ken Mawatari and Takashi Kojima for useful discussions about the details of SED fitting and the N/O abundance ratio, respectively. This research is supported by NAOJ ALMA Scientific Research Grant number 2020-16B and by JSPS KAKENHI Grant Number 17H01114. TH was supported by Leading Initiative for Excellent Young Researchers, MEXT, Japan (HJH02007). EZ acknowledges funding from the Swedish National Space Agency. This paper makes use of the following ALMA data: ADS/JAO.ALMA#2019.1.01491.S. ALMA is a partnership of ESO (representing its member states), NSF (USA), and NINS (Japan), together with NRC (Canada), MOST and ASIAA (Taiwan), and KASI (Republic of Korea), in cooperation with the Republic of Chile. The Joint ALMA Observatory is operated by ESO, AUI/NRAO, and NAOJ. This research has made use of NASA's Astrophysics Data System.

Software: CASA (McMullin et al. 2007), NumPy (Harris et al. 2020), SciPy (Virtanen et al. 2020), IPython (Perez & Granger 2007), Matplotlib (Hunter 2007), Astropy (Astropy Collaboration et al. 2013, 2018), APLpy (Robitaille & Bressert 2012), CLOUDY (Ferland et al. 2017), PyNeb (Luridiana et al. 2015)

REFERENCES

- Abel, N. P., Ferland, G. J., Shaw, G., & van Hoof, P. A. M. 2005, *ApJS*, 161, 65, doi: [10.1086/432913](https://doi.org/10.1086/432913)
- Andrews, B. H., & Martini, P. 2013, *ApJ*, 765, 140, doi: [10.1088/0004-637X/765/2/140](https://doi.org/10.1088/0004-637X/765/2/140)
- Appleton, P. N., Guillard, P., Boulanger, F., et al. 2013, *ApJ*, 777, 66, doi: [10.1088/0004-637X/777/1/66](https://doi.org/10.1088/0004-637X/777/1/66)
- Asplund, M., Grevesse, N., Sauval, A. J., & Scott, P. 2009, *ARA&A*, 47, 481, doi: [10.1146/annurev.astro.46.060407.145222](https://doi.org/10.1146/annurev.astro.46.060407.145222)
- Astropy Collaboration, Robitaille, T. P., Tollerud, E. J., et al. 2013, *A&A*, 558, A33, doi: [10.1051/0004-6361/201322068](https://doi.org/10.1051/0004-6361/201322068)
- Astropy Collaboration, Price-Whelan, A. M., Sipőcz, B. M., et al. 2018, *AJ*, 156, 123, doi: [10.3847/1538-3881/aabc4f](https://doi.org/10.3847/1538-3881/aabc4f)
- Bakx, T. J. L. C., Tamura, Y., Hashimoto, T., et al. 2020, *MNRAS*, 493, 4294, doi: [10.1093/mnras/staa509](https://doi.org/10.1093/mnras/staa509)
- Baldwin, J. A., Phillips, M. M., & Terlevich, R. 1981, *PASP*, 93, 5, doi: [10.1086/130766](https://doi.org/10.1086/130766)
- Boselli, A., Gavazzi, G., Lequeux, J., & Pierini, D. 2002, *A&A*, 385, 454, doi: [10.1051/0004-6361:20020156](https://doi.org/10.1051/0004-6361:20020156)
- Bouwens, R. J., Aravena, M., Decarli, R., et al. 2016, *ApJ*, 833, 72, doi: [10.3847/1538-4357/833/1/72](https://doi.org/10.3847/1538-4357/833/1/72)
- Bowler, R. A. A., Bourne, N., Dunlop, J. S., McLure, R. J., & McLeod, D. J. 2018, *MNRAS*, 481, 1631, doi: [10.1093/mnras/sty2368](https://doi.org/10.1093/mnras/sty2368)
- Bowler, R. A. A., Dunlop, J. S., McLure, R. J., et al. 2014, *MNRAS*, 440, 2810, doi: [10.1093/mnras/stu449](https://doi.org/10.1093/mnras/stu449)
- Capak, P. L., Carilli, C., Jones, G., et al. 2015, *Nature*, 522, 455, doi: [10.1038/nature14500](https://doi.org/10.1038/nature14500)
- Carilli, C. L., & Walter, F. 2013, *ARA&A*, 51, 105, doi: [10.1146/annurev-astro-082812-140953](https://doi.org/10.1146/annurev-astro-082812-140953)
- Carniani, S., Maiolino, R., Pallottini, A., et al. 2017, *A&A*, 605, A42, doi: [10.1051/0004-6361/201630366](https://doi.org/10.1051/0004-6361/201630366)
- Carniani, S., Maiolino, R., Amorin, R., et al. 2018, *MNRAS*, 478, 1170, doi: [10.1093/mnras/sty1088](https://doi.org/10.1093/mnras/sty1088)
- Carniani, S., Ferrara, A., Maiolino, R., et al. 2020, *MNRAS*, 499, 5136, doi: [10.1093/mnras/staa3178](https://doi.org/10.1093/mnras/staa3178)
- Chabrier, G. 2003, *PASP*, 115, 763, doi: [10.1086/376392](https://doi.org/10.1086/376392)
- Cheng, C., Cao, X., Lu, N., et al. 2020, *ApJ*, 898, 33, doi: [10.3847/1538-4357/ab980b](https://doi.org/10.3847/1538-4357/ab980b)
- Cormier, D., Madden, S. C., Lebouteiller, V., et al. 2015, *A&A*, 578, A53, doi: [10.1051/0004-6361/201425207](https://doi.org/10.1051/0004-6361/201425207)

- Cormier, D., Abel, N. P., Hony, S., et al. 2019, *A&A*, 626, A23, doi: [10.1051/0004-6361/201834457](https://doi.org/10.1051/0004-6361/201834457)
- Cunningham, D. J. M., Chapman, S. C., Aravena, M., et al. 2020, *MNRAS*, 494, 4090, doi: [10.1093/mnras/staa820](https://doi.org/10.1093/mnras/staa820)
- da Cunha, E., Groves, B., Walter, F., et al. 2013, *ApJ*, 766, 13, doi: [10.1088/0004-637X/766/1/13](https://doi.org/10.1088/0004-637X/766/1/13)
- De Breuck, C., Weiß, A., Béthermin, M., et al. 2019, *A&A*, 631, A167, doi: [10.1051/0004-6361/201936169](https://doi.org/10.1051/0004-6361/201936169)
- De Looze, I., Cormier, D., Lebouteiller, V., et al. 2014, *A&A*, 568, A62, doi: [10.1051/0004-6361/201322489](https://doi.org/10.1051/0004-6361/201322489)
- Decarli, R., Walter, F., Carilli, C., et al. 2014, *ApJL*, 782, L17, doi: [10.1088/2041-8205/782/2/L17](https://doi.org/10.1088/2041-8205/782/2/L17)
- Eldridge, J. J., Stanway, E. R., Xiao, L., et al. 2017, *PASA*, 34, e058, doi: [10.1017/pasa.2017.51](https://doi.org/10.1017/pasa.2017.51)
- Erb, D. K., Shapley, A. E., Pettini, M., et al. 2006, *ApJ*, 644, 813, doi: [10.1086/503623](https://doi.org/10.1086/503623)
- Fanciullo, L., Kemper, F., Scicluna, P., Dharmawardena, T. E., & Srinivasan, S. 2020, *MNRAS*, 499, 4666, doi: [10.1093/mnras/staa2911](https://doi.org/10.1093/mnras/staa2911)
- Farrah, D., Lebouteiller, V., Spoon, H. W. W., et al. 2013, *ApJ*, 776, 38, doi: [10.1088/0004-637X/776/1/38](https://doi.org/10.1088/0004-637X/776/1/38)
- Ferland, G. J., Korista, K. T., Verner, D. A., et al. 1998, *PASP*, 110, 761, doi: [10.1086/316190](https://doi.org/10.1086/316190)
- Ferland, G. J., Chatzikos, M., Guzmán, F., et al. 2017, *RMxAA*, 53, 385. <https://arxiv.org/abs/1705.10877>
- Fudamoto, Y., Oesch, P. A., Faisst, A., et al. 2020, arXiv e-prints, arXiv:2004.10760. <https://arxiv.org/abs/2004.10760>
- Fujimoto, S., Oguri, M., Brammer, G., et al. 2021, arXiv e-prints, arXiv:2101.01937. <https://arxiv.org/abs/2101.01937>
- Fukui, Y., Kawamura, A., Minamidani, T., et al. 2008, *ApJS*, 178, 56, doi: [10.1086/589833](https://doi.org/10.1086/589833)
- Furusawa, H., Kashikawa, N., Kobayashi, M. A. R., et al. 2016, *ApJ*, 822, 46, doi: [10.3847/0004-637X/822/1/46](https://doi.org/10.3847/0004-637X/822/1/46)
- Harikane, Y., Ouchi, M., Inoue, A. K., et al. 2020, *ApJ*, 896, 93, doi: [10.3847/1538-4357/ab94bd](https://doi.org/10.3847/1538-4357/ab94bd)
- Harris, C. R., Jarrod Millman, K., van der Walt, S. J., et al. 2020, *Nature*, 585, 357, doi: [10.1038/s41586-020-2649-2](https://doi.org/10.1038/s41586-020-2649-2)
- Hashimoto, T., Laporte, N., Mawatari, K., et al. 2018, *Nature*, 557, 392, doi: [10.1038/s41586-018-0117-z](https://doi.org/10.1038/s41586-018-0117-z)
- Hashimoto, T., Inoue, A. K., Mawatari, K., et al. 2019, *PASJ*, 71, 71, doi: [10.1093/pasj/psz049](https://doi.org/10.1093/pasj/psz049)
- Hayashi, M., Ly, C., Shimasaku, K., et al. 2015, *PASJ*, 67, 80, doi: [10.1093/pasj/psv041](https://doi.org/10.1093/pasj/psv041)
- Herrera-Camus, R., Sturm, E., Graciá-Carpio, J., et al. 2018a, *ApJ*, 861, 95, doi: [10.3847/1538-4357/aac0f9](https://doi.org/10.3847/1538-4357/aac0f9)
- . 2018b, *ApJ*, 861, 94, doi: [10.3847/1538-4357/aac0f6](https://doi.org/10.3847/1538-4357/aac0f6)
- Hunter, J. D. 2007, *Computing in Science and Engineering*, 9, 90, doi: [10.1109/MCSE.2007.55](https://doi.org/10.1109/MCSE.2007.55)
- Inoue, A. K., Hashimoto, T., Chihara, H., & Koike, C. 2020, arXiv e-prints, arXiv:2004.12612. <https://arxiv.org/abs/2004.12612>
- Inoue, A. K., Shimizu, I., Tamura, Y., et al. 2014, *ApJL*, 780, L18, doi: [10.1088/2041-8205/780/2/L18](https://doi.org/10.1088/2041-8205/780/2/L18)
- Inoue, A. K., Tamura, Y., Matsuo, H., et al. 2016, *Science*, 352, 1559, doi: [10.1126/science.aaf0714](https://doi.org/10.1126/science.aaf0714)
- Iono, D., Yun, M. S., Elvis, M., et al. 2006, *ApJL*, 645, L97, doi: [10.1086/506344](https://doi.org/10.1086/506344)
- Jones, T., Sanders, R., Roberts-Borsani, G., et al. 2020, arXiv e-prints, arXiv:2006.02447. <https://arxiv.org/abs/2006.02447>
- Kashino, D., Silverman, J. D., Sanders, D., et al. 2017, *ApJ*, 835, 88, doi: [10.3847/1538-4357/835/1/88](https://doi.org/10.3847/1538-4357/835/1/88)
- Kauffmann, G., Heckman, T. M., Tremonti, C., et al. 2003, *MNRAS*, 346, 1055, doi: [10.1111/j.1365-2966.2003.07154.x](https://doi.org/10.1111/j.1365-2966.2003.07154.x)
- Kennicutt, Jr., R. C. 1998, *ARA&A*, 36, 189, doi: [10.1146/annurev.astro.36.1.189](https://doi.org/10.1146/annurev.astro.36.1.189)
- Kewley, L. J., Dopita, M. A., Leitherer, C., et al. 2013, *ApJ*, 774, 100, doi: [10.1088/0004-637X/774/2/100](https://doi.org/10.1088/0004-637X/774/2/100)
- Knudsen, K. K., Watson, D., Frayer, D., et al. 2017, *MNRAS*, 466, 138, doi: [10.1093/mnras/stw3066](https://doi.org/10.1093/mnras/stw3066)
- Kojima, T., Ouchi, M., Nakajima, K., et al. 2017, *PASJ*, 69, 44, doi: [10.1093/pasj/psx017](https://doi.org/10.1093/pasj/psx017)
- Laporte, N., Ellis, R. S., Boone, F., et al. 2017, *ApJL*, 837, L21, doi: [10.3847/2041-8213/aa62aa](https://doi.org/10.3847/2041-8213/aa62aa)
- Larson, R. B. 1981, *MNRAS*, 194, 809, doi: [10.1093/mnras/194.4.809](https://doi.org/10.1093/mnras/194.4.809)
- Le Fèvre, O., Béthermin, M., Faisst, A., et al. 2019, arXiv e-prints, arXiv:1910.09517. <https://arxiv.org/abs/1910.09517>
- Lee, M. M., Nagao, T., De Breuck, C., et al. 2019, *ApJL*, 883, L29, doi: [10.3847/2041-8213/ab412e](https://doi.org/10.3847/2041-8213/ab412e)
- Leitherer, C., Schaerer, D., Goldader, J. D., et al. 1999, *ApJS*, 123, 3, doi: [10.1086/313233](https://doi.org/10.1086/313233)
- Lequeux, J., Peimbert, M., Rayo, J. F., Serrano, A., & Torres-Peimbert, S. 1979, *A&A*, 500, 145
- Li, J., Wang, R., Cox, P., et al. 2020, *ApJ*, 900, 131, doi: [10.3847/1538-4357/ababac](https://doi.org/10.3847/1538-4357/ababac)
- Loaiza-Agudelo, M., Overzier, R. A., & Heckman, T. M. 2020, *ApJ*, 891, 19, doi: [10.3847/1538-4357/ab6f6b](https://doi.org/10.3847/1538-4357/ab6f6b)
- Luridiana, V., Morisset, C., & Shaw, R. A. 2015, *A&A*, 573, A42, doi: [10.1051/0004-6361/201323152](https://doi.org/10.1051/0004-6361/201323152)
- Madau, P., & Dickinson, M. 2014, *ARA&A*, 52, 415, doi: [10.1146/annurev-astro-081811-125615](https://doi.org/10.1146/annurev-astro-081811-125615)
- Madden, S. C., Rémy-Ruyer, A., Galametz, M., et al. 2013, *PASP*, 125, 600, doi: [10.1086/671138](https://doi.org/10.1086/671138)
- Maiolino, R., Carniani, S., Fontana, A., et al. 2015, *MNRAS*, 452, 54, doi: [10.1093/mnras/stv1194](https://doi.org/10.1093/mnras/stv1194)
- Marrone, D. P., Spilker, J. S., Hayward, C. C., et al. 2018, *Nature*, 553, 51, doi: [10.1038/nature24629](https://doi.org/10.1038/nature24629)
- Masters, D., McCarthy, P., Siana, B., et al. 2014, *ApJ*, 785, 153, doi: [10.1088/0004-637X/785/2/153](https://doi.org/10.1088/0004-637X/785/2/153)

- McMullin, J. P., Waters, B., Schiebel, D., Young, W., & Golap, K. 2007, in *Astronomical Society of the Pacific Conference Series*, Vol. 376, *Astronomical Data Analysis Software and Systems XVI*, ed. R. A. Shaw, F. Hill, & D. J. Bell, 127
- Meurer, G. R., Heckman, T. M., & Calzetti, D. 1999, *ApJ*, 521, 64, doi: [10.1086/307523](https://doi.org/10.1086/307523)
- Nagao, T., Maiolino, R., De Breuck, C., et al. 2012, *A&A*, 542, L34, doi: [10.1051/0004-6361/201219518](https://doi.org/10.1051/0004-6361/201219518)
- Nagao, T., Maiolino, R., Marconi, A., & Matsuhara, H. 2011, *A&A*, 526, A149, doi: [10.1051/0004-6361/201015471](https://doi.org/10.1051/0004-6361/201015471)
- Novak, M., Bañados, E., Decarli, R., et al. 2019, *ApJ*, 881, 63, doi: [10.3847/1538-4357/ab2beb](https://doi.org/10.3847/1538-4357/ab2beb)
- Page, B. E. J. 2009, *Nucleosynthesis and Chemical Evolution of Galaxies*
- Pavesi, R., Riechers, D. A., Capak, P. L., et al. 2016, *ApJ*, 832, 151, doi: [10.3847/0004-637X/832/2/151](https://doi.org/10.3847/0004-637X/832/2/151)
- Pentericci, L., Carniani, S., Castellano, M., et al. 2016, *ApJL*, 829, L11, doi: [10.3847/2041-8205/829/1/L11](https://doi.org/10.3847/2041-8205/829/1/L11)
- Perez, F., & Granger, B. E. 2007, *Computing in Science and Engineering*, 9, 21, doi: [10.1109/MCSE.2007.53](https://doi.org/10.1109/MCSE.2007.53)
- Pilyugin, L. S., Grebel, E. K., & Mattsson, L. 2012, *MNRAS*, 424, 2316, doi: [10.1111/j.1365-2966.2012.21398.x](https://doi.org/10.1111/j.1365-2966.2012.21398.x)
- Remijan, A. J., Markwick-Kemper, A., & ALMA Working Group on Spectral Line Frequencies. 2007, in *American Astronomical Society Meeting Abstracts*, Vol. 211, *American Astronomical Society Meeting Abstracts*, 132.11
- Robitaille, T., & Bressert, E. 2012, *APLpy: Astronomical Plotting Library in Python*. <http://ascl.net/1208.017>
- Russell, R. W., Melnick, G., Gull, G. E., & Harwit, M. 1980, *ApJL*, 240, L99, doi: [10.1086/183332](https://doi.org/10.1086/183332)
- Salpeter, E. E. 1955, *ApJ*, 121, 161, doi: [10.1086/145971](https://doi.org/10.1086/145971)
- Sanders, R. L., Shapley, A. E., Kriek, M., et al. 2016, *ApJ*, 816, 23, doi: [10.3847/0004-637X/816/1/23](https://doi.org/10.3847/0004-637X/816/1/23)
- Sanders, R. L., Shapley, A. E., Reddy, N. A., et al. 2020, *MNRAS*, 491, 1427, doi: [10.1093/mnras/stz3032](https://doi.org/10.1093/mnras/stz3032)
- Schaerer, D., Ginolfi, M., Bethermin, M., et al. 2020, arXiv e-prints, arXiv:2002.00979. <https://arxiv.org/abs/2002.00979>
- Shapley, A. E., Coil, A. L., Ma, C.-P., & Bundy, K. 2005, *ApJ*, 635, 1006, doi: [10.1086/497630](https://doi.org/10.1086/497630)
- Shapley, A. E., Reddy, N. A., Kriek, M., et al. 2015, *ApJ*, 801, 88, doi: [10.1088/0004-637X/801/2/88](https://doi.org/10.1088/0004-637X/801/2/88)
- Shivaei, I., Reddy, N. A., Siana, B., et al. 2018, *ApJ*, 855, 42, doi: [10.3847/1538-4357/aaad62](https://doi.org/10.3847/1538-4357/aaad62)
- Spilker, J. S., Marrone, D. P., Aravena, M., et al. 2016, *ApJ*, 826, 112, doi: [10.3847/0004-637X/826/2/112](https://doi.org/10.3847/0004-637X/826/2/112)
- Stanway, E. R., & Eldridge, J. J. 2018, *MNRAS*, 479, 75, doi: [10.1093/mnras/sty1353](https://doi.org/10.1093/mnras/sty1353)
- Steidel, C. C., Strom, A. L., Pettini, M., et al. 2016, *ApJ*, 826, 159, doi: [10.3847/0004-637X/826/2/159](https://doi.org/10.3847/0004-637X/826/2/159)
- Steidel, C. C., Rudie, G. C., Strom, A. L., et al. 2014, *ApJ*, 795, 165, doi: [10.1088/0004-637X/795/2/165](https://doi.org/10.1088/0004-637X/795/2/165)
- Strom, A. L., Steidel, C. C., Rudie, G. C., Trainor, R. F., & Pettini, M. 2018, *ApJ*, 868, 117, doi: [10.3847/1538-4357/aae1a5](https://doi.org/10.3847/1538-4357/aae1a5)
- Strom, A. L., Steidel, C. C., Rudie, G. C., et al. 2017, *ApJ*, 836, 164, doi: [10.3847/1538-4357/836/2/164](https://doi.org/10.3847/1538-4357/836/2/164)
- Tamura, Y., Mawatari, K., Hashimoto, T., et al. 2019, *ApJ*, 874, 27, doi: [10.3847/1538-4357/ab0374](https://doi.org/10.3847/1538-4357/ab0374)
- Tielens, A. G. G. M., & Hollenbach, D. 1985, *ApJ*, 291, 722, doi: [10.1086/163111](https://doi.org/10.1086/163111)
- Veilleux, S., & Osterbrock, D. E. 1987, *ApJS*, 63, 295, doi: [10.1086/191166](https://doi.org/10.1086/191166)
- Vila-Costas, M. B., & Edmunds, M. G. 1993, *MNRAS*, 265, 199, doi: [10.1093/mnras/265.1.199](https://doi.org/10.1093/mnras/265.1.199)
- Vincenzo, F., Belfiore, F., Maiolino, R., Matteucci, F., & Ventura, P. 2016, *MNRAS*, 458, 3466, doi: [10.1093/mnras/stw532](https://doi.org/10.1093/mnras/stw532)
- Virtanen, P., Gommers, R., Oliphant, T. E., et al. 2020, *Nature Methods*, 17, 261, doi: [10.1038/s41592-019-0686-2](https://doi.org/10.1038/s41592-019-0686-2)
- Watson, D., Christensen, L., Knudsen, K. K., et al. 2015, *Nature*, 519, 327, doi: [10.1038/nature14164](https://doi.org/10.1038/nature14164)
- Yabe, K., Ohta, K., Iwamuro, F., et al. 2014, *MNRAS*, 437, 3647, doi: [10.1093/mnras/stt2185](https://doi.org/10.1093/mnras/stt2185)

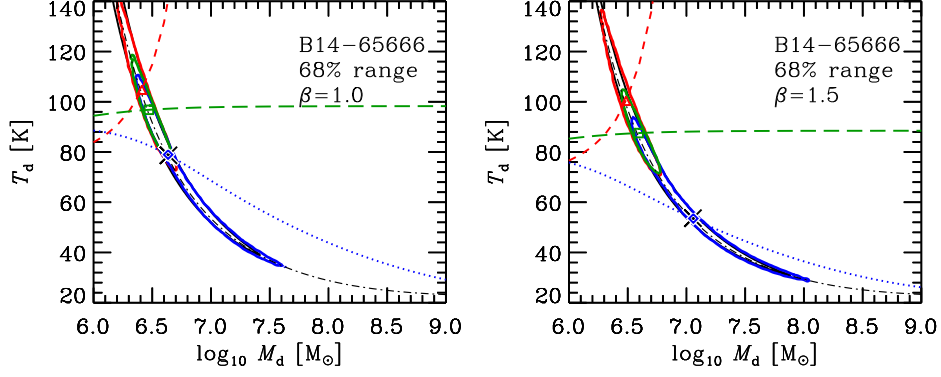


Figure 11. Same as Figure 4 but for the emissivity indices $\beta = 1.0$ and 1.5 .

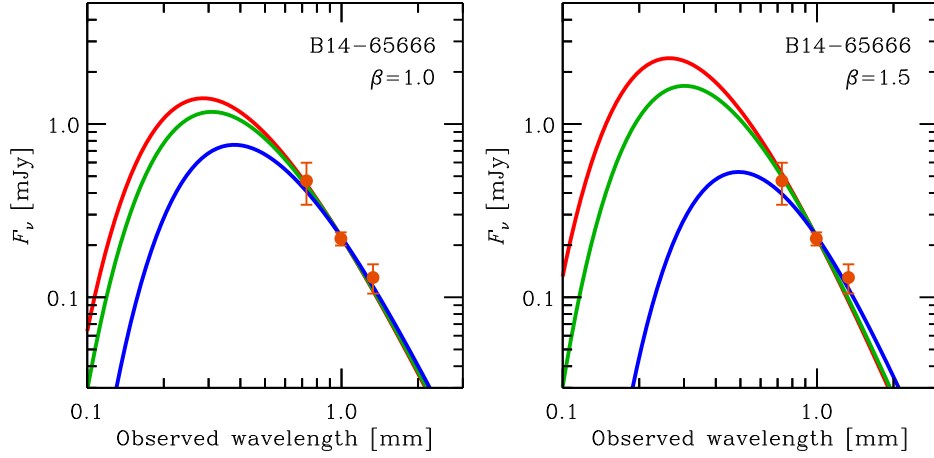


Figure 12. Same as Figure 4 but for the emissivity indices $\beta = 1.0$ and 1.5 .

APPENDIX

A. RESULTS OF THE RADIATIVE EQUILIBRIUM FITTING DEPENDING ON β

FIR SED fitting depends on the assumed emissivity index β . The results for $\beta = 2.0$ is shown in the main text. Figure 11 shows the fitting results of the radiative equilibrium algorithm and Figure 12 shows the best-fit FIR SEDs in the case of $\beta = 1.0$ and 1.5 . Figure 13 shows the distribution of the solutions in the clumpy geometry for $\beta = 1.0$ and 1.5 . Table A1 summarizes the results of FIR SED fitting, including the modified blackbody fitting.

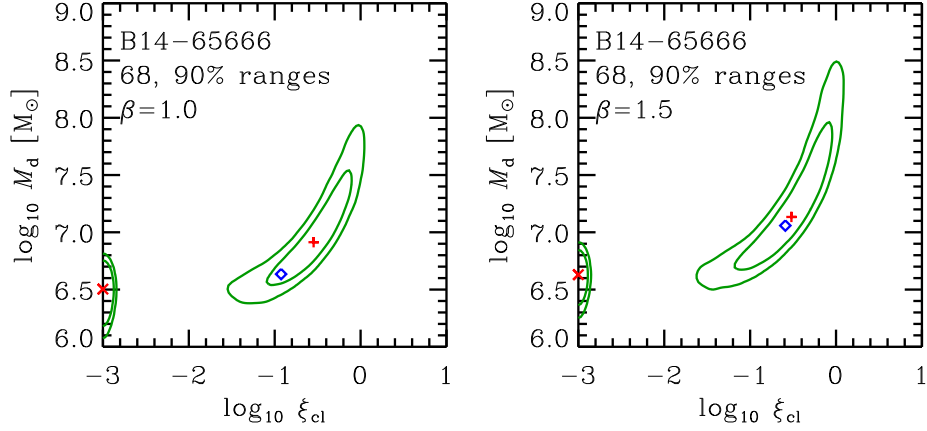


Figure 13. Same as Figure 4 but for the emissivity indices $\beta = 1.0$ and 1.5 . In these cases, the crosses are the highest peaks, and the plus signs are the second highest peaks.

Table A1. A summary of the FIR SED fitting results.

Cases	χ^2	d.o.f.	T_d		$\log_{10} \xi_{cl}$	$\log_{10}(L_{IR}/L_{\odot})$	SFR_{IR} ($M_{\odot} \text{ yr}^{-1}$)
			(K)	$\log_{10}(M_d/M_{\odot})$			
(1)	(2)	(3)	(4)	(5)	(6)	(7)	(8)
Modified blackbody fitting							
$\beta = 2.0$	1.45	1	40.8 (29.2–61.5)	7.45 (6.96–8.06)	—	11.62 (11.35–12.19)	72
$\beta = 1.5$	1.07	1	53.7 (36.5–95.5)	7.06 (6.52–7.57)	—	11.80 (11.39–12.64)	110
$\beta = 1.0$	0.74	1	78.7 (47.4–255)	6.64 (5.86–7.15)	—	12.09 (11.50–13.86)	210
Radiative equilibrium fitting, shell model							
$\beta = 2.0$	4.53	2	96.6 (79.8–131)	6.55 (6.33–6.71)	—	12.97 (12.62–13.55)	1600
$\beta = 1.5$	2.19	2	100 (82.6–137)	6.49 (6.27–6.64)	—	12.72 (12.41–13.25)	900
$\beta = 1.0$	0.88	2	105 (86.0–142)	6.41 (6.20–6.56)	—	12.49 (12.21–12.95)	530
Radiative equilibrium fitting, homogeneous model							
$\beta = 2.0$	3.62	2	79.7 (71.8–91.5)	6.71 (6.59–6.81)	—	12.63 (12.44–12.87)	730
$\beta = 1.5$	1.85	2	87.5 (78.0–102)	6.59 (6.47–6.69)	—	12.50 (12.32–12.75)	540
$\beta = 1.0$	0.82	2	96.8 (85.2–115)	6.47 (6.34–6.58)	—	12.37 (12.19–12.62)	400
Radiative equilibrium fitting, clumpy model							
$\beta = 2.0$	1.45	1	40.7 (27.7–64.4)	7.45 (6.91–8.21)	-0.43 (-1.09–-0.11)	11.62 (11.42–12.45)	72
$\beta = 1.5$	1.07	1	53.5 (35.0–82.5)	7.06 (6.64–7.65)	-0.59 (< -0.19)	11.79 (11.40–12.43)	110
$\beta = 1.0$	0.74	1	79.0 (45.8–99.8)	6.63 (6.44–7.20)	-0.93 (< -0.31)	12.09 (11.48–12.42)	210

NOTE— The values in the parentheses indicate the 68 percent ranges around the best-fit values. For the modified blackbody fitting, both dust temperature, T_d , and dust mass, M_d , are the fitting parameters. For the radiative equilibrium fitting, T_d and M_d are connected and only one of them is the actual fitting parameter. In the clumpy model, another fitting parameter — the clumpiness, ξ_{cl} — is introduced. The IR luminosity, L_{IR} , is a derived quantity. The IR star formation rate, SFR_{IR} , is derived from L_{IR} with the conversion of Kennicutt (1998).